First published: 08 August 2023
https://doi.org/10.1002/smll.202305104

Bridging a Gap in Thermal Conductivity and Heat Transfer in Hybrid Fibers and Yarns via Polyimide and Silicon Nitride Composites

Ahmadreza Moradi[1], *Piotr K. Szewczyk*[1], *Urszula Stachewicz*[1*]

[1] Faculty of Metals Engineering and Industrial Computer Science, AGH University of Krakow, 30-059 Krakow, Poland

*Corresponding author, e-mail address: ustachew@agh.edu.pl

KEYWORDS:
Yarn Electrospinning, Scanning thermal microscopy, Thermal conductive fibers, nanocomposites, Polyimide, Silicon nitride

Abstract

The pressing issues of the energy crisis and rapid electronics development have sparked a growing interest in the production of highly thermally conductive polymer composites. Due to the challenges related to the poor processability of hybrid materials and filler distribution to achieve high thermal conductivity, we employed electrospinning to create composite nanofibers and yarns using polyimide (PI) and thermally conductive silicon nitride (SiN) nanoparticles. The thermal performance of the individual nanofibers was evaluated using scanning thermal microscopy (SThM), providing significant insights into their heat transfer performance. Next, we applied the nanofibers as coatings on resistance wires to assess the thermal conductivity and insulation properties. Notably, the samples containing 35 wt% of SiN exhibited a 25 % increase in surface temperature. These innovative materials hold great promise as exceptional candidates for smart textiles and thermal management applications, addressing the growing demand for effective heat dissipation and regulation.

1. Introduction

Due to the rapid population expansion and environmental concerns, problems related to the energy crisis have become one of the most urgent issues in the 21st century, which lends itself to the development of thermal management and energy storage systems.[1,2] Polymer materials characterized by lightweight, good electrical insulation performance, flexibility, and design freedom are good candidates for these applications.[3,4] However, the low intrinsic thermal conductivity significantly limits their applicability where fast heat conduction is needed. Thus, new polymer-based structures, and hybrid materials, with enhanced thermal conductivity are in high demand.[5,6] Among the different approaches for increasing polymers' thermal conductivity, adding thermally conductive fillers to the polymer matrix is the most effective method. Nonetheless, achieving high thermal conductivity in most cases needs high filler content, which can be problematic for processability. Besides, the uniform distribution of particles is another concern that can negatively affect mechanical properties.[7–9]

Hexagonal boron nitride nanosheet (h-BNNS) with high thermal conductivity up to 600 $Wm^{-1}K^{-1}$, is one of the often utilized ceramic fillers to enhance thermal conductivity.[10] However, h-BNNs is prepared by direct synthesis or exfoliation methods, which is very challenging to obtain high yields and low structural of the nanosheets.[11] Boron nitride (BN) in the form of nanoparticles is commercially available yet its thermal conductivity is not as high as h-BNNS, up to 180-200 $Wm^{-1}K^{-1}$.[12,13] The other nitride base filler that has been used for enhancing the thermal conductivity of composites is silicon nitride (SiN),[14] with the thermal conductivity up to 180 $Wm^{-1}K^{-1}$, close to BN particles, but importantly it is commercially available in reduced cost and smaller size of around 50 nm compared to BN nanoparticles reaching 150 nm in diameter.[13]

Electrospinning is a versatile method for producing polymer fiber meshes, membranes, and composite fibers in a single step.[15,16] It also effectively improves filler distribution, even at high concentrations, and achieves directional arrangement along polymer fibers.[17] This addresses a major challenge in fabricating thermally conductive nanocomposites.[2,18] The fillers' organization during electrospinning directly affects the polymer chains' alignment and reorientation, which increases the thermal conductivity and Young's modulus of produced fibers.[19,20]

This research aims to enhance the thermal conductivity of polymer nanofibers and yarns by adding thermally conductive nanofillers. We electrospun composite nanofibers by incorporating SiN nanoparticles into a polyimide (PI) matrix. Polyimide (PI) is regarded as one

of the most promising engineering polymers due to its excellent thermal stability, chemical resistance, radiation resistance, and mechanical properties. Its exceptional heat resistance is particularly desirable for heat transfer applications, as it effectively maintains its structural integrity even when is exposed to high temperatures.[21,22] Varying concentrations of nanoparticles were employed to fabricate hybrid nanofibers, enabling us to investigate the influence of nanoparticle content on morphology, thermal conductivity, and mechanical properties. Importantly, scanning thermal microscopy (SThM) and thermal camera imaging were employed to assess the thermal properties. A crucial element of our approach was the ability to establish a correlation between individual nanofibers' thermal conductivity and the resulting yarns' performance. Based on our findings, we identified the most suitable hybrid system for thermal management applications.

2. Results and discussion

2.1. Nanofiber's morphology and density

The electrospun mats based on just PI and mixed with 15, 25, and 35 wt% of SiN nanoparticles in relation to PI amount were prepared and named PISiN15, PISiN25, and PISiN35, respectively. The concentration of PI and electrospinning parameters were kept the same for all the randomly deposited samples. By comparing the morphology of composite and PI nanofibers, see **Figure 1**-a, the SiN nanoparticles were visible in the form of agglomerates and protruded from the PI nanofibers, which made the nanofibers' surface rougher. Figure 1-b shows that nanofibers loaded with higher concentrations of nanoparticles had lower average diameters, from 369 to 350 nm, which was affected by the higher conductivity of solutions.[23] However, further addition of SiN from 25 to 35 wt% resulted in slightly thicker nanofibers, owing to the higher viscosity of the PISiN35 solution compared to the PISiN25 solution. Additionally, Figure 1-c displays a rise in the density of the electrospun nanofibers as the concentration of SiN increased, showing that the nanoparticles are uniformly dispersed into the polymer solution and adequately incorporated into the electrospun membranes. Moreover, the EDS results (Figure 1-d-e and Figure S1) confirmed the excellent nanoparticles distribution in polymer nanofibers and the formation of a continuous network along the axial direction of nanofibers. The large contact area between the SiN nanoparticles is expected to form thermally conductive paths with lower thermal resistance when heat is transferred through the composite nanofibers. Therefore, more dense thermal pathways can be formed using a higher mass fraction of SiN.[13]

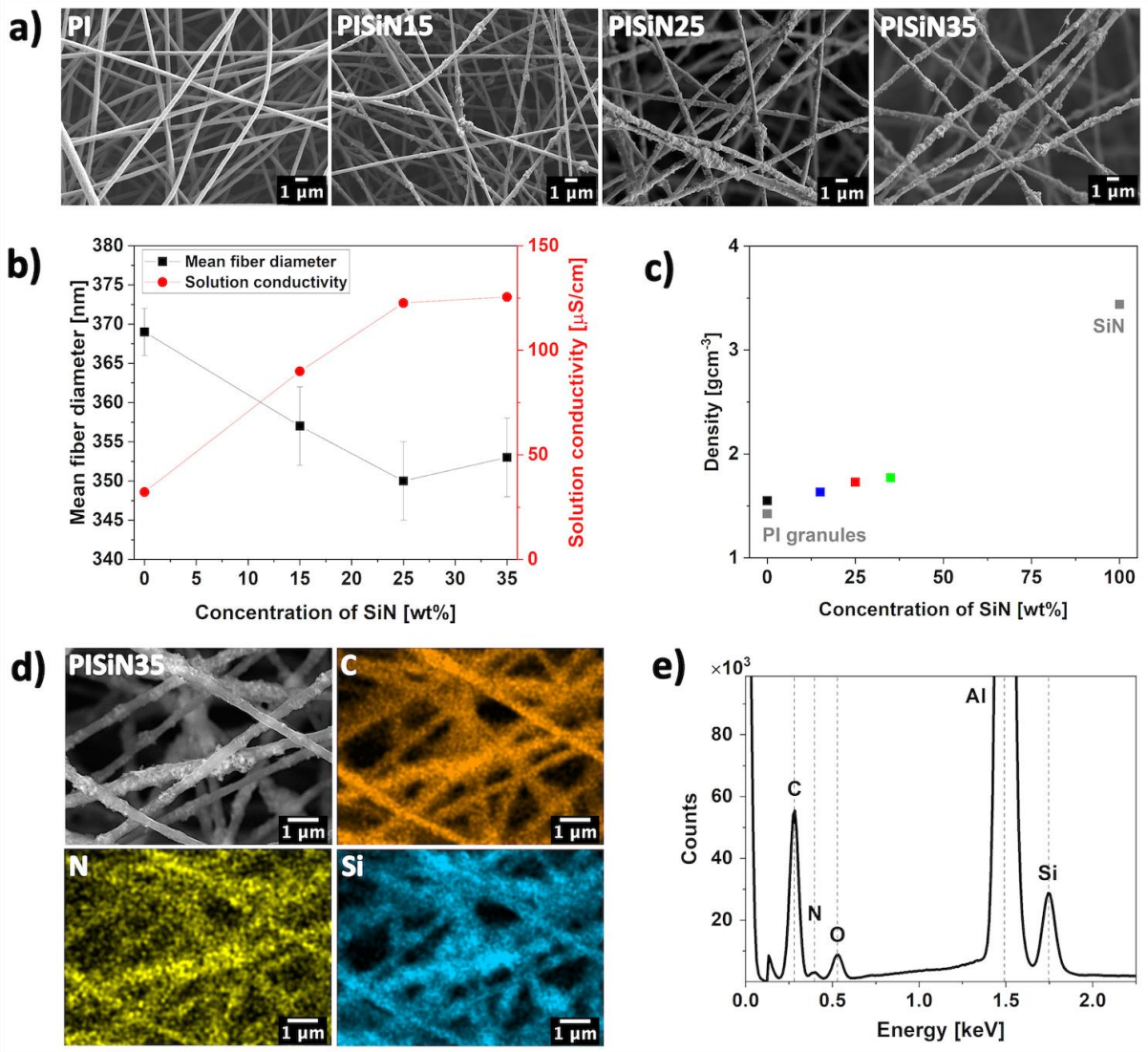

Figure 1. a) SEM micrographs showing the morphologies of electrospun PI nanofibers with different concentrations of SiN, b) conductivity of PI and PISiN solutions prior to electrospinning, and mean nanofiber diameter of the samples as a function of SiN concentration, c) the measured density of the PI granules and electrospun PI and PISiN nanofibers, d) SEM micrograph and EDS mapping images of C, N, and Si elements with e) corresponding EDS spectrum of PISiN35 nanofibers.

2.2. Chemical analysis and mechanical properties

The chemical structure of the electrospun meshes and SiN nanoparticles was identified by ATR-FTIR, see **Figure 2**-a. The characteristic absorption bands of imide ring deformation and OC-N-CO appeared at 721 cm^{-1} and 1096 cm^{-1}, respectively. The bands at 1362 cm^{-1} show the C-N stretch, and at 1721 cm^{-1} are related to the C=O stretch.[24–26] Moreover, the broad peak

at 844 cm^{-1} demonstrates the Si-N stretch band in the spectrum of SiN nanoparticles.[27] It can be seen in Figure 2-b that an increase in the SiN concentration resulted in peaks with higher intensity in the region 780 cm^{-1} – 1100 cm^{-1}, proving the presence of nanoparticles in the electrospun nanofibers.

Additionally, Figure 2-c represents the stress-strain curves of the nanofiber meshes. The inclusion of 15 wt% SiN nanoparticles in the PI nanofibers improved tensile strength, reaching 205 kPa (Figure 2-e). This observation is consistent with previous reports that suggest the inclusion of nanoparticles, which serve as a stiffer component within polymer fibers, can effectively enhance the mechanical properties of the composite. This improvement can be attributed to load transfer mechanisms and stress dissipation phenomena.[28] Moreover, nanoparticles can retard crack propagation in fibers.[29] However, further increase of the SiN concentrations to 25 wt% and 35 wt% reduced the σ_{max} of PI meshes by 5.5 and 9.6 %.

Higher concentrations of SiN led to an increased formation of nanoparticle agglomerates, which act as stress concentration points and introduce structural defects within the composite meshes.[28,30–32] As is evident in Figure 2-d, the breakage of the composite nanofibers happened around the nanoparticle agglomerates, which supports the observed mechanical performance of the samples. However, the addition of the nanoparticles also deteriorated the ductility of the meshes as the strain at maximum stress (ε_{max}) and strain at failure decreased with the increase of SiN concentration. Lower ductility is owing to the low plastic deformation of ceramic SiN nanoparticles and the presence of nanoparticle agglomerates which interlock the nanofibers in the mesh network and limit their movement and reorientation in the direction of the load.[28,33] Nevertheless, all the meshes showed high strain before failure, over 150 %, which shows good stretchability of the samples. In addition, the decrease in mechanical strength is below 10 %, which shows the effectiveness of the electrospinning method for producing composite nanofibers with high concentrations of nanoparticles.

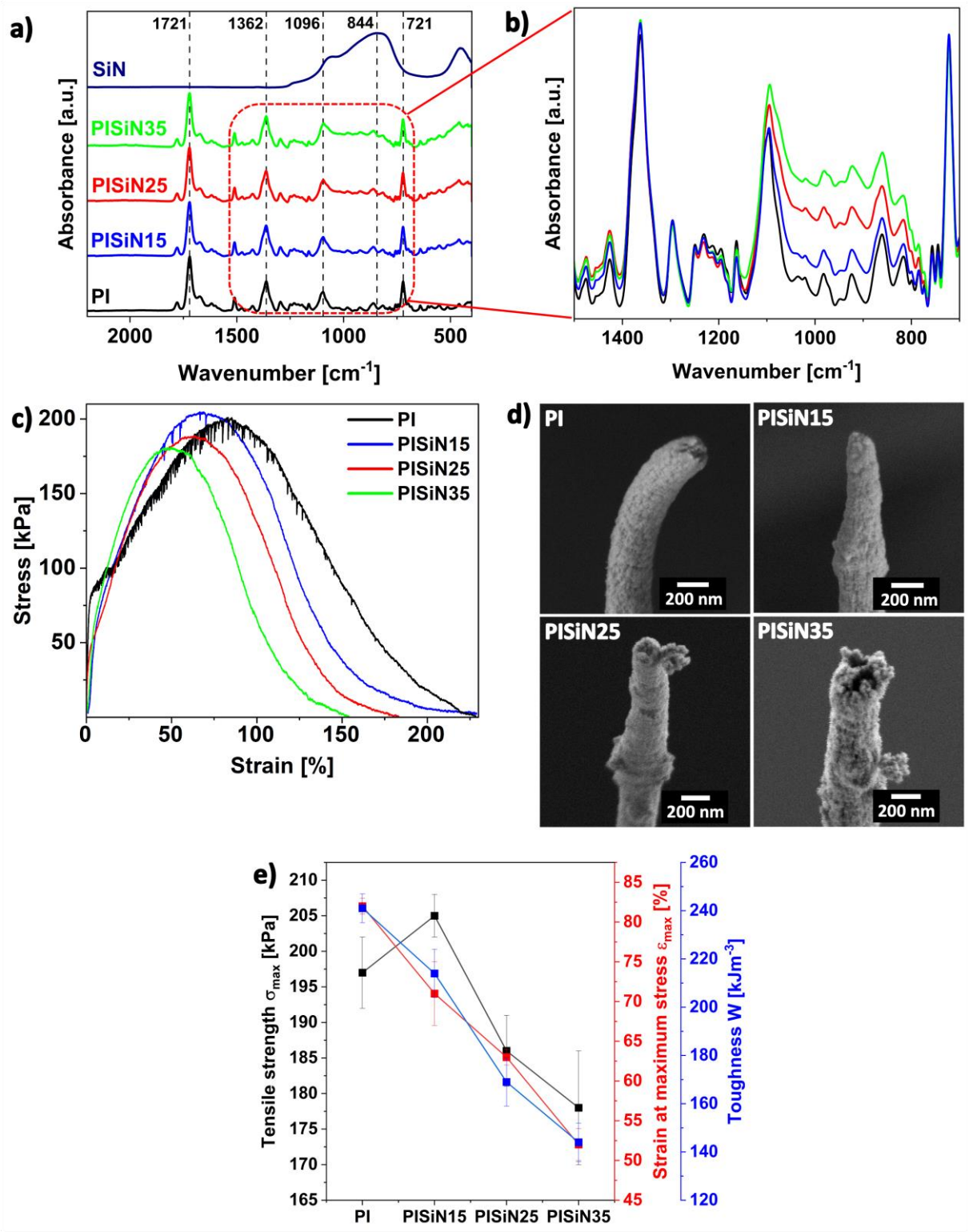

Figure 2. a) The ATR-FTIR spectra of the electrospun samples and SiN powder, with data vertically shifted for better comparison. b) The magnified ATR-FTIR spectra of the electrospun samples in the region 700-1500 cm^{-1}, without the vertical shift of data. c) Stress-strain curves of the electrospun mats, d) SEM micrographs of the fractured nanofibers of PI, PISiN15, PISiN25, and PISiN35, after the mechanical test. e) Summary of the mechanical properties of the electrospun PI and PISiN mats.

2.3. Thermal analysis - Scanning thermal microscopy

Recently, the number of works related to improving the thermal conductivity of electrospun membranes has increased dramatically, necessitating the development of a proper and accurate method for measuring the thermal conductivity of the produced membranes. Among the existing techniques, laser flash point and hot disk methods have been widely used for measuring thermal conductivity.[23,34–36] However, accurate thermal conductivity measurement of thin electrospun membranes, often having porosity around 90 %,[37,38] is still a pending and challenging issue. Problems such as reaching a thermal equilibrium state in a short time, laser penetration depth close to the film's thickness, direct contact of the film and the sample holder, and large thermal contact resistance between the heating source and the thin film are the main reasons that increase the measurement error for very thin films.[39,40] Besides, the measurement error is even higher for electrospun membranes due to their high porosity and high anisotropic thermal conductivity, especially with thermally conductive fillers. Another disadvantage is the necessity of usually applying carbon-based coating on the polymer membranes that, in the case of thin samples, artificially increases the measured thermal conductivity values.[14] Wang et al.[13] and Zhang et al.[14] coated both sides of their produced membranes with graphite powder before measuring the thermal conductivity. They used the laser flash method and reported high in-plane thermal conductivities of 25 $Wm^{-1}K^{-1}$ and 7.29 $Wm^{-1}K^{-1}$, respectively. Apart from the thermal performance of porous membranes, measuring the thermal conductivity and assessing the thermal properties of individual fibers is crucial for building hierarchical structures. So far, all the methods for increasing the thermal conductivity of polymers are focused on improving the microstructural order of the polymer matrix to reduce phonon diffraction.[13] Therefore, examining the thermal characteristics of individual micro/nanofibers allows us to gain an important understanding of the mechanisms of heat transfer at a submicron level. It clarifies the thermal dynamics and transfers mechanisms within larger structures such as membranes, yarns, and textiles.

Here the SThM method was used to investigate the thermal conductivity and heat transfer in electrospun polymer composite nanofibers. SThM is an accurate and effective method for mapping the thermal conductivity of materials with high spatial thermal resolution (< 50 nm) and thermal sensitivity (< 0.01 °C).[41,42] In the thermal conductivity contrast mode of SThM (**Figure 3**-a), the AFM laser heats the cantilever, and the thermocouple monitors the

temperature at its tip. By changing the laser's position on the cantilever, the temperature can be adjusted to a desired amount up to the limitation of the probe. Then, the tip is raster scanned over the sample.

The temperature of the tip is measured as it moves and creates a map that combines thermal information with the sample's surface features. The thermal distribution map is directly linked to the thermal conductivity of the regions on the sample. This correlation arises from the increased heat dissipation between the tip and sample in places with higher thermal conductivity, leading to a lower temperature at the tip. However, it should be noted that although SThM is an excellent technique for investigating the local thermal phenomena at the nanoscale, it still cannot provide the quantitative values for the thermal conductivity of the materials. Figure 3-b shows examples of output data obtained from one pixel on the nanofiber and one pixel on the ITO glass, colored as black and red dots on the spectroscopy line, respectively. Next, Figure 3-c displays the average temperature recorded at the cantilever's tip while it was in contact with nanofibers and located on the top of the sample. The temperature of the tip, observed on the composite nanofibers, was lower than the pristine PI nanofibers, indicating that the addition of SiN nanoparticles led to an increased thermal conductivity within nanofibers. While EDS mapping images revealed the presence of an interconnected network of SiN, it is worth noting that not all particles were exposed on the nanofiber surface. In fact, nanoparticles can also be found embedded within the polymer nanofibers. Therefore, the SThM spectroscopy measurement was done with randomly placed lines on many nanofibers to ensure all measurements, including regions with and without nanoparticle agglomerates. Notably, we measured the temperature gradient on the nanometer scale, and a change as small as 0.5 °C can still be translated to large changes in the thermal conductivity of the material, which we showed in the case of yarns.[43]

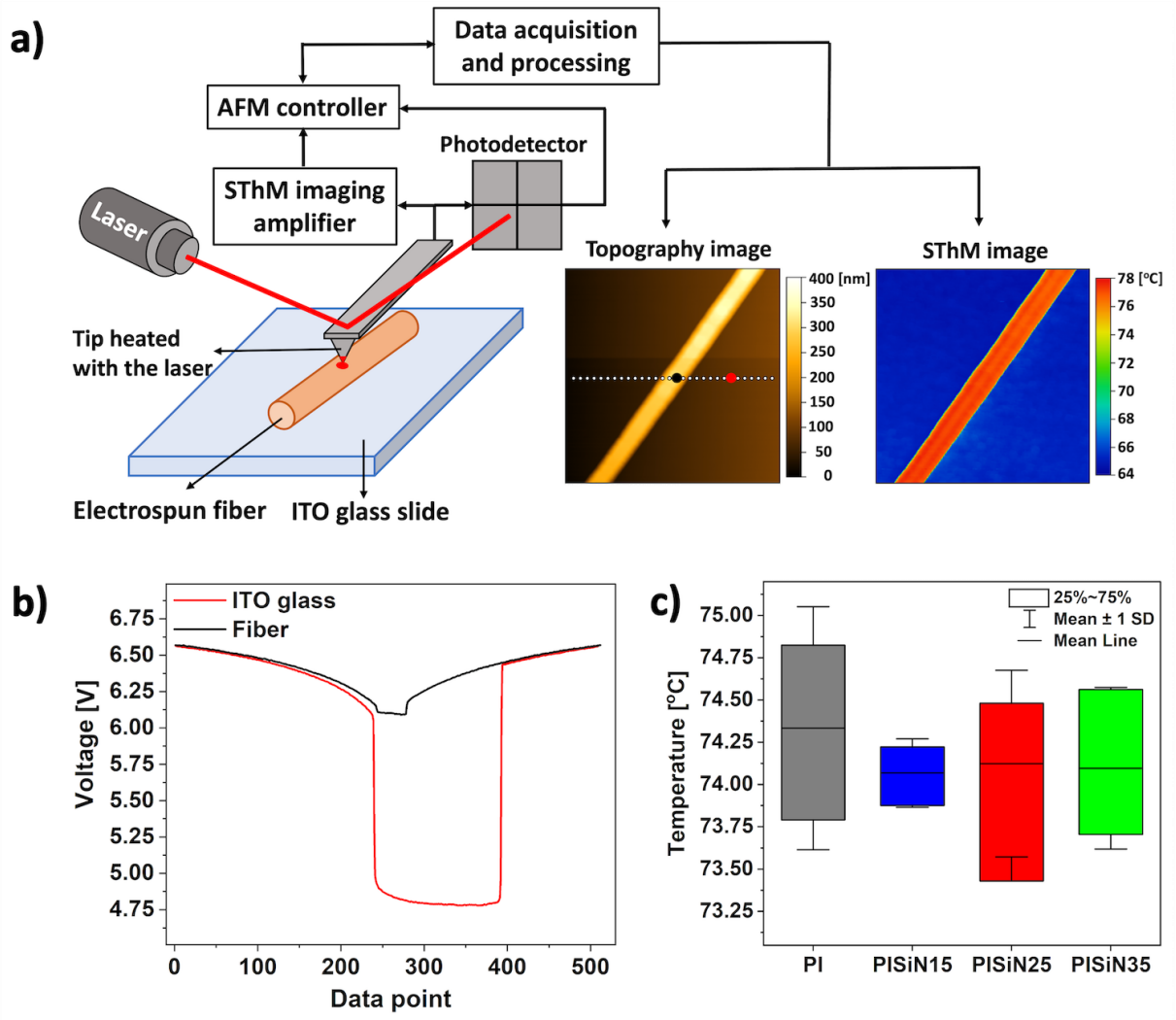

Figure 3. a) A schematic diagram of an AFM integrated with an SThM module, b) an example of obtained output voltages from one point on the nanofiber and one point on the background (black and red pixels on the topography image), c) The average temperature of the tip on individual nanofibers for samples containing 15, 25 and 35% of SiN nanoparticles.

2.4. Yarn electrospinning and thermal camera measurement

To create yarns, a combination of a resistance wire as the core and electrospun nanofibers as the coating was employed. This process involved electrospinning equipment with a dedicated yarn module, where nanofibers were carefully wrapped around the resistance metal wire and subsequently guided through the vortex collector. (**Figure 4**-a, and Movie S1). The obtained electrospun coating yarns on the wire are presented in Figure 4-b and Figure S2-a-a". It is apparent that the electrospun nanofibers exhibited a general alignment and twisting pattern along the resistance wire, as depicted in Figure 4-c and Figure S2-b-b". The overall thickness

of the yarns, considering both the wire and coating, fell within the range of 600-800 μm, as indicated in Table S1. The nanofibers within the yarns displayed a morphology similar to those prepared as a mat using a single nozzle, as shown in Figure 4-d and Figure S2-c-c". However, the nanofiber diameter in the yarns was slightly smaller, ranging from 200-400 nm, as illustrated in Figure S3.

Further, the resistance wire was used as the core connected to the heating source to evaluate the thermal properties and performance of the electrospun yarns. The applied current to the wires was set so that the maximum temperature on the control surface, a standard tape, reached 80 °C, recorded by the thermal camera, see Figure 4-e and Figure S4. The presence of SiN nanoparticles in the PI nanofiber caused an increase in the surface temperature of the composite yarns. As shown in Figure 4-f, contrary to the individual nanofibers, here the change in the temperature is more significant, up to 25 % higher for the sample with 35 wt% of SiN, and follows an upward trend as the concentration of SiN nanoparticles increases. The results can be attributed to the intricate arrangement of nanofibers in yarns, comprising numerous tightly intertwined hybrid nanofibers. This structural configuration enables the effective interlinking of nanofibers, facilitating the formation of interconnected thermal conductive networks composed of SiN nanoparticles. This compact and twisted structure of nanofibers into yarns results in further improvement in the thermal conductivity of the system, especially in the through-plane direction, which is very challenging regarding the electrospun membranes.[31,34,35] Electrospun composites membranes have low through-plane thermal conductivity because of high porosity, meaning that most of the structure consists of air which is an insulating material with a low conductivity coefficient of about 0.03 $Wm^{-1}K^{-1}$. [44] Besides, owing to high porosity, there is a lack of sufficient connections between nanofibers to form thermal conduction paths. To overcome these problems, post-processing methods like hot pressing the electrospun membranes or a combination of electrospinning and electrospraying methods have been used.[34,36,45–47]

For instance, Yang et al.[31] used the combination of electrospinning and hot pressing to produce thermally conductive composites based on polyvinyl alcohol (PVA) and boron nitride nanosheets (BNNS - 30 wt%). The composite film showed a surface temperature of 70°C, around 8°C higher than PVA film on the hot plate with a temperature of 75°C. Guo et al.[23] prepared composite films based on carbon nanotubes pillared grew on exfoliated graphite (CPEG – 10 wt%) and PI with electrospinning, lay-up, and hot pressing. The composite film showed a surface temperature around 95°C, so 10°C higher than the PI film on the hotplate set to 105°C. Also, thermal conductive composites based on PVA and alumina (Al_2O_3 – 65 wt%)

were fabricated by Wei et al.[48] using electrospinning. The composite membrane showed an 8°C higher surface temperature on the hotplate with 90°C compared to the PVA membrane. Comparing the heat transfer capability of the produced composites proves challenging due to variations in conditions, sample sizes, and geometries during the measurements. An additional concern arises when employing a hot press to generate a coating or film that exhibits reduced porosity and pore sizes. However, the notable temperature differences observed between the membranes with and without the conductive fillers demonstrate the successful enhancement of thermal conductivity in the composites. Likewise, within this study, the temperature difference of 15°C between PISiN35 and PI yarns highlights the significantly greater thermal conductivity and heat dissipation capacity of the hybrid nanofiber-based yarns in comparison to PI yarns. Furthermore, the one-step manufacturing process of yarn coating using electrospinning can be more or at least equally effective as post-processing techniques in enhancing the through-plane thermal conductivity of the electrospun structure. Unlike previous studies that often-required additional hot pressing, this step is not necessary in this particular case. Moreover, textile materials based on composite nanofiber yarns generally exhibit superior mechanical properties compared to electrospun membranes.[49,50] They are also more user-friendly and find excellent utility in wearable electronics, thermoregulating textiles, and sensor applications. Notably, by utilizing yarns with carefully adjusted porosity, we can still maintain their breathability, which is advantageous over hot-pressed approaches.[51,52]

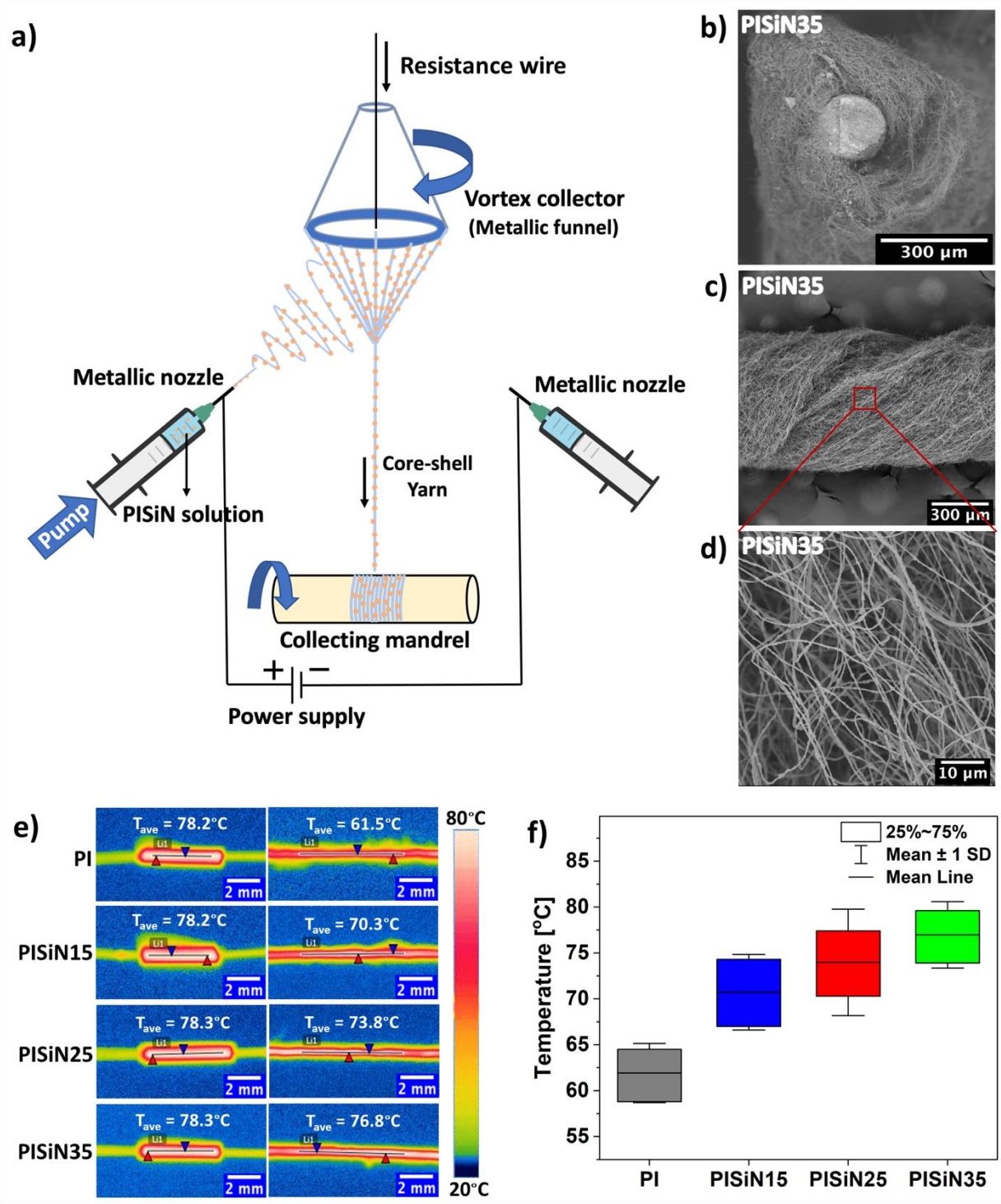

Figure 4. a) Schematic illustration of the yarn fabrication process, b-d) SEM micrographs of the cross-sectional and the surface morphology of PISiN35 yarns on the metal wire, e) infrared images of standard tapes, on the left, and the yarns, on the right, with the average lines of temperature, f) the average surface temperature of the yarns with different concentrations of SiN.

To further underline the significance of the obtained results for PI-SiN hybrid nanofiber yarns, we performed additional simulations of thermal conductivity for solid and porous coatings applied on the metal wire, see **Figure 5**. Figure 5-a represents the temperature distribution in the PI and PISiN35 yarns resulting from heat transfer simulation. Here, the thermal conductivity used for PISiN35 yarns was calculated by the parallel model, which generally gives the upper limit for the thermal conductivity of composites.[12,34,45] The simulation results consistently correlate with the experimental findings, revealing that composite materials exhibit elevated surface temperatures attributed to their higher thermal conductivity. Nevertheless, even with 80% porosity, the surface temperatures in the simulations exceed the measured temperatures obtained from thermal camera measurements. This discrepancy can be attributed to the ideal thermal contact assumed between the resistance wire and the coating in the simulations. In contrast, in the yarns utilized in our experiments, thermal conductivity is limited by factors such as thermal contact resistance and nanofiber diameters and orientations, which can reduce thermal conductivity.[18] As shown in Figure 5-b, porosity is one factor that lowers the heat conduction in the yarns and coatings, and its effect is more pronounced when the material has low thermal conductivity. However, it also can be used as an adjusting tool for the thermal conduction capacity of composites and hybrid materials.[53] Therefore, it is another advantage of using electrospinning to produce fibrous coatings as the porosity of yarns can be easily adjusted with the rotation speeds of the vortex and collecting mandrel and tailored for the intended applications.[54,55] Furthermore, the simulation shows that the surface temperature for hybrid PISiN35 coatings is almost independent of the porosity in a steady state condition, see Figure 5 b. These results demonstrate a significant advantage in the construction of smart textiles utilizing the developed yarns presented in this study. PI-SiN hybrid nanofiber yarns and coatings are bridging the gap in thermal conductivity and heat transfer, allowing the potential applications development in the thermal management and thermal energy harvesting systems based on smart textiles and small devices.

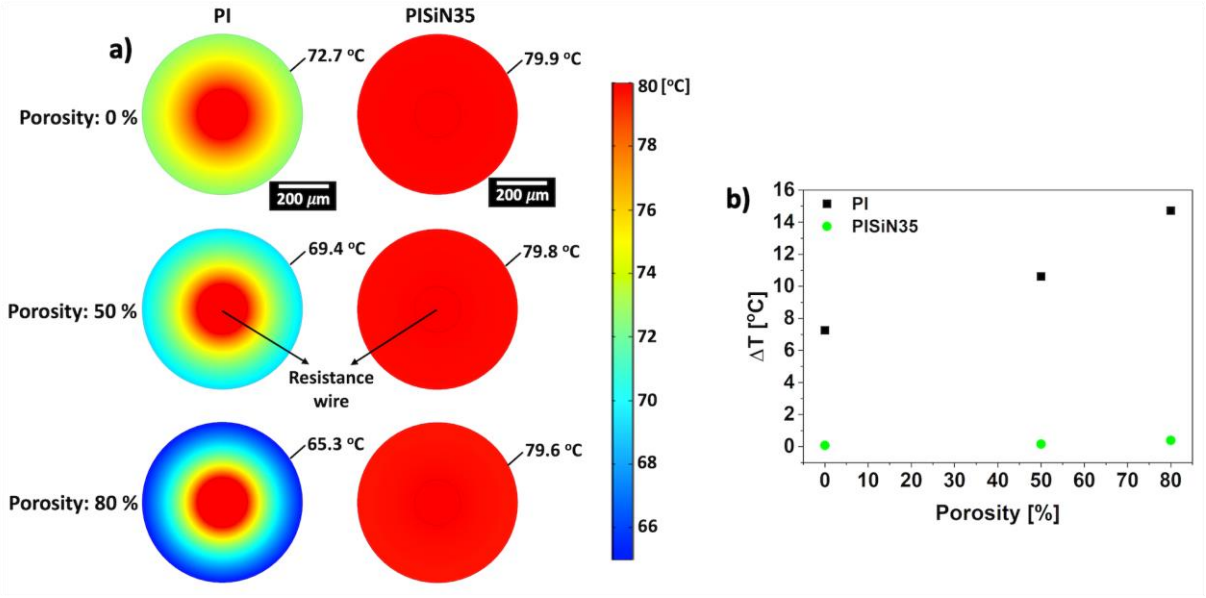

Figure 5. The heat transfer simulation inside the yarns with the polymer coating on the resistance metal wire, a) the temperature distribution in the PI and PISiN35 yarns with no porosity, 50 %, and 80 % porosity. b) the temperature difference between the surface of the resistance wire and the yarns as a function of porosity.

3. Conclusions

We have successfully created hybrid nanofibers and yarns through electrospinning, incorporating SiN nanoparticles into PI to enhance their thermal conductivity. The SiN nanoparticles were evenly dispersed within the electrospun nanofibers and yarns, establishing interconnected networks of thermal conduction pathways within the composites. This integration of SiN into the PI nanofibers bolstered the electrospun membranes' tensile strength and maintained the composites' exceptional stretchability. A significant breakthrough was achieved by utilizing the thermal spectroscopy mode of atomic force microscopy (AFM) to evaluate the thermal performance of individual nanofibers. The results demonstrated notably improved thermal conductivity. Further, the heat conduction capabilities of the electrospun yarns were justified on resistance wire by employing the thermal camera. We proved that the introduction of SiN nanoparticles into the system led to a substantial increase in the surface temperature of the yarns, about 25 %, confirming the effective enhancement of thermal conductivity through nanofibers arrangements and contact. Moreover, theoretical considerations further supported the experimental findings, highlighting the advantages of the porous yarn structure in achieving a balanced thermal conductivity that can be tailored for

specific applications. The developed and manufactured yarns in this study, featuring enhanced heat conduction capacity, hold great promise for a wide range of applications, including thermal management of electronics, thermoregulating textiles, wearable electronics, and sensors, among many others.

4. Materials and Methods

4.1. Sample preparation – electrospinning

For producing the electrospun fibers, PI (TECAPOWDER PI SG granulates, M_w = 114262 $gmol^{-1}$, PDI = 1.8, Ensinger Sintimid GmbH, Austria) was dried for 4 h at 50 °C (Drying Oven, POL-ECO Aparatura, Poland) prior to solution preparation. PI (16 wt%) was dissolved in dimethylacetamide (DMAc) and dimethyl sulfoxide (DMSO) in a 7:3 mass ratio by stirring on a heating plate (IKA, Germany) at a speed of 250 rpm for 18 h. For the solutions with SiN nanoparticles (particle size <50 nm, density: 3.44 gml^{-1}, Sigma Aldrich, UK), first, we homogenized the nanoparticles in DMAc:DMSO in an ultrasonic bath (Sonorex Bandelin, Germany) for 2 h, then the PI granulate was added to the suspensions and stirred for 18 h at a speed of 250 rpm. The solutions containing SiN nanoparticles were ultrasonicated for 2 h prior to the electrospinning. The conductivity of the solutions was measured using a conductometer (Mettler Toledo SevenCompact S210, Zurich, Switzerland) equipped with a conductivity probe (InLab 720). The solutions were electrospun using equipment with a climate control chamber (SKE Research Equipment, Italy) at relative humidity (RH) = 45% and temperature (T) = 25 °C. The rest of the electrospinning parameters were: applied voltage of 20 kV, flow rate of 0.2 mlh^{-1}, 21-gauge stainless steel nozzle, and nozzle to collector distance of 18 cm. For the mechanical test, the solutions were electrospun for 30 min on laser-cut paper frames with rectangular holes (20×8 mm) mounted on a cylindrical collector (rotation speed of 40 rpm).

The yarns with the core (resistance wire, RD 100/0,2 Block, Germany) and nanofibers as coating-shell yarns were fabricated using electrospinning equipment with yarn module (TechNOVA, China) at RH = 36-42% and T = 25 °C. The positive high voltage of 10-14 kV was applied to the nozzle with the polymer solutions, and the negative high voltage of 10-12 kV was applied to the second nozzle. The distance of the positive and negative nozzles to the vortex collector was set to 15-18 cm and 17-18 cm, respectively. The flow rate of the solutions

was 0.007-0.015 $mLmin^{-1}$, and the rotation speeds of the vortex and collecting mandrel were 150 and 7 rpm, respectively.

4.2. Scanning electron microscopy

The morphology of the produced samples was characterized using scanning electron microscopy (SEM, Merlin Gemini II, ZEISS, Germany). The samples were covered with an 8 nm layer of Au by a sputter coater (Q150RS, Quorum Technologies, UK). The imaging was done at 2-3 kV accelerating voltage and 3.9-6.1 mm working distance using an SE detector. The average nanofiber diameters (D_f) were calculated from 100 randomly chosen nanofibers from SEM images using ImageJ software (v. 1.53d, USA). To study the distribution of nanoparticles, elemental mapping using energy-dispersive X-ray spectroscopy (EDS, Brucker, Germany) was done. The samples were coated with a thin layer of C ($\simeq$ 15 nm) by a carbon evaporator (K950, Emitech (Quorum Technologies), UK), and the mapping was carried out for 500 s, at 15 kV, 550 pA, and 6-7 mm working distance, utilizing backscattered electron detector. Morphology and cross-section of the yarns were investigated by SEM (Phenom ProX, Thermo Fisher Scientific, USA) at an accelerating voltage of 10 kV. For cross-section imaging, the samples were prepared by the freeze-fracture method in liquid nitrogen.

4.3. FTIR and gas pycnometry

The chemical composition of the obtained samples was analyzed by Attenuated Total Reflectance – Fourier Transform Infrared Spectroscopy (ATR-FTIR, Nicolet™ iS™ 5, Thermo Fisher Scientific, USA) with the diamond crystal. During measurements, the spectra were averaged over 32 scans in the 400 – 4000 cm^{-1} range, with a resolution of 4 cm^{-1}. The baseline was created and subtracted from the spectra, and the spectra were normalized using the Peak Analyzer and normalize functions in OriginPro (2021b, USA), respectively.

We used a gas pycnometer (AccuPyc 1330 He, Micromeritics, Norcross, GA, USA) to measure the density of the electrospun samples and PI granules. The device was equipped with a 1 cm^3 cylinder cell, and the average density was calculated from 10 measurements.

4.4. Mechanical test

We used a tensile machine equipped with a 20N cell (Kammrath & Weiss, Dortmund, Germany) to assess the mechanical properties of the electrospun meshes. The tests were carried out at T = 20-25 °C and RH = 35-45 %, with an extension rate of 25 μms^{-1}. The stress was calculated as a force measured by the machine divided by the initial cross-section of the electrospun mats. The averaged thickness of the samples was measured using a light microscope (Axio Imager M1m, ZEISS, Germany) imaging in the z-direction from 5 different points on the samples. The average values for toughness (W), maximum stress (σ_{max}), and strain at maximum stress (ε_{max}) were calculated from three separate measurements using Integrate function in OriginPro software. In addition, the morphology of the nanofibers before and after the mechanical test was studied by SEM.

4.5. Scanning thermal microscopy

An atomic force microscope (AFM, CoreAFM, Nanosurf, Switzerland) with scanning thermal microscopy (SThM, VertiSense^{TM}, AppNano, USA) module was used for the thermal analysis of individual nanofibers. The samples were prepared by short electrospinning on the indium tin oxide-coated glass slide (ITO glass) attached to the collector. A proper adhesion between the sample and the background substrate is essential to obtain an accurate thermal map with high resolution. However, this can be challenging for electrospun fibers due to the accumulation of electrostatic charges on the fibers during the electrospinning process and their lightweight. Thus, ITO glass was used as the background substrate for the measurements. The conductive layer of indium tin oxide results in less charge accumulation and better adhesion between the nanofibers and the background. We used a VTP-375 thermal probe with a silicon cantilever with 0.95 $N.m^{-1}$ spring constant and a hollow silicon dioxide tip integrated with a 50 nm thermocouple at the apex of the tip. The laser heated the cantilever tip, and its temperature was set in the range of 85-86 °C before contact with the samples. The ITO glasses were attached to the metallic stage using a silver paste to have a thermal path for heat dissipation. The measurements were carried out in spectroscopy mode over several lines for each sample. Each line with a size of 10-20 μm was divided into 32 pixels. At each pixel, the tip approached and contacted the sample, then retracted, and the temperature on the tip was recorded as the change in the thermocouple's voltage. The time and amplitude for the approach and retraction of the tip were set to 2 μm and 1.5 s, respectively, and the amount of force as a stop-by value was 20 nN. For calculating the average temperature of the nanofibers, only the measurements related to pixels on the nanofibers when the tip was in contact, the second plateaued region with minimum values on

the nanofiber's output voltage diagram in Figure 3-b, were chosen. The same thermal probe was used for conducting all the measurements to avoid any thermal transport variation related to the probe. All the measurements were done in ambient conditions.

4.6. Thermal camera

The electrospun yarns (length of 15 cm) were heated up by applying current to the resistance wires (diameter of 200 μm), and the surface temperature of the yarns was captured by a thermal camera (FLIR T560, USA); see Figure S4. A standard tape with a constant emissivity of 0.96 was attached to the wires to control that all the resistance wires had the same temperature. The average surface temperatures were calculated using average lines in FLIR Tools software from five separate measurements. The infrared images were taken at T = 22-24°C and RH = 24-25 %.

4.7. Modeling (Simulation of heat transfer in core-shell yarns)

The simulation of heat transfer in the PI and PISiN35 core-shell yarns was performed by COMSOL Multiphysics (version 5.6, COMSOL Inc., Sweden). Due to the high length-to-diameter ratio of the yarns used in thermal camera measurements, the temperature was assumed to change only in the radial direction. Thus, 3D models of yarns were simplified to 2D models consisting of two concentric circles as the resistance wire and electrospun yarns, The diameter of the resistance wire was set to 200 μm, and the diameters of PI and PISiN35 yarns, which were obtained from SEM images (Figure 4-c and Figure S2-b), were set to 640 and 700 μm respectively. Since the electrospun yarns are porous, the heat transfer in the porous media interface was used to make the simulations closer to reality. The thermal conductivity of the resistive wire, PI yarns, and PISiN35 yarns were set to 23 $Wm^{-1}K^{-1}$, 0.11 $Wm^{-1}K^{-1}$, and 13.7 $Wm^{-1}K^{-1}$, respectively. A constant temperature of 80 °C was added to the resistance wire as the heating source. The heat transfer coefficient of convective heat flux was calculated as 35.1 $Wm^{-1}K^{-1}$, the surface emissivity of the yarns was 0.96, and the ambient temperature was set to 22 °C. The simulation results presented in Figure 5, were performed at the stationary conditions after reaching the temperature equilibrium. Additionally, in the Supporting Information, Figure S5, we added the analysis in the time-dependent conditions for the porosity level at 50% for PI and PiSiN35 yarns.

Conflict of interest

The authors declare that they have no known competing financial interests or personal relationships that could have appeared to influence the work reported in this paper. The raw/processed data required to reproduce this finding are available on request.

Author contributions

All authors contributed to the preparation of the paper. A.M. performed the experiments, analyzed the results, and wrote the paper. P.K.S. contributed to designing experiments, characterization of the materials, and editing the paper. U.S. supervised the overall research, secured funding and resources, discussed the results, wrote, reviewed, and edited the paper.

Supporting Information

Supporting Information is available from the Wiley Online Library or from the author.

In the supporting information, we provided SEM micrographs of PI and PISiN nanofibers together with their EDS mapping images and corresponding EDS spectra (Figure S1), SEM micrographs of the cross-section and surface morphology of PI and PISiN yarns (Figure S2), The fiber diameter distribution diagrams of the PI and PISiN nanofibers in the single nozzle and yarn electrospinning processes (Figure S3), the schematic diagram of the setup used for assessing the thermal performance of the electrospun yarns (Figure S4), the thickness of the electrospun yarns (Table S1) and the heat transfer simulation as a function of time (Figure S5).

Acknowledgments

This study was conducted as part of the BioCom4SavEn project funded by the European Research Council under the European Union's Horizon 2020 Framework Programme for Research and Innovation (ERC grant agreement no. 948840).

References

[1] F. Kong, J. Yan, C. Zhang, W. Yang, K. Wang, C. Zhang, T. Shao, *ACS Appl. Mater. Interfaces* **2023**, *15*, 16009.

[2] W.-H. Han, Q.-Y. Wang, Y.-Y. Kang, X. Zhou, C.-C. Hao, *Nanoscale* **2023**, *15*, 2003.

[3] Z. Wei, P. Gong, X. Kong, M. Li, J. Cheng, H. Zhou, D. Li, Y. Ye, X. Lu, J. Yu, S. Lu, *ACS Appl. Nano Mater.* **2023**, *6*, 8358.

[4] C. Tan, Z. Dong, Y. Li, H. Zhao, X. Huang, Z. Zhou, J.-W. Jiang, Y.-Z. Long, P. Jiang, T.-Y. Zhang, B. Sun, *Nat. Commun.* **2020**, *11*, 3530.

[5] X. Zhang, B. Xie, S. Zhou, X. Yang, Y. Fan, R. Hu, X. Luo, *Nano Energy* **2022**, *104*, 107986.

[6] C.-P. Feng, F. Wei, K.-Y. Sun, Y. Wang, H.-B. Lan, H.-J. Shang, F.-Z. Ding, L. Bai, J. Yang, W. Yang, *Nano-Micro Lett.* **2022**, *14*, 127.

[7] Y. Murtaja, L. Lapčík, H. Sepetcioglu, J. Vlček, B. Lapčíková, M. Ovsík, M. Staněk, *Nanotechnol. Rev.* **2022**, *11*, 312.

[8] S. Zhou, Y. Shi, Y. Bai, M. Liang, H. Zou, *Polym. Compos.* **2020**, *41*, 5418.

[9] M. H. Al-Saleh, U. Sundararaj, *Compos. Part A Appl. Sci. Manuf.* **2011**, *42*, 2126.

[10] W. Wu, M. Zheng, K. Lu, F. Liu, Y.-H. Song, M. Liu, Z.-M. Dang, *Compos. Part A Appl. Sci. Manuf.* **2023**, *169*, 107533.

[11] M. R. H. Mazumder, L. D. Mathews, S. Mateti, N. V Salim, J. Parameswaranpillai, P. Govindaraj, N. Hameed, *Appl. Mater. Today* **2022**, *29*, 101672.

[12] H. Chen, V. V. Ginzburg, J. Yang, Y. Yang, W. Liu, Y. Huang, L. Du, B. Chen, *Prog. Polym. Sci.* **2016**, *59*, 41.

[13] Y. Guo, K. Ruan, X. Shi, X. Yang, J. Gu, *Compos. Sci. Technol.* **2020**, *193*, 108134.

[14] A. Khan, M. Puttegowda, P. Jagadeesh, H. M. Marwani, A. M. Asiri, A. Manikandan, A. A. Parwaz Khan, G. M. Ashraf, S. M. Rangappa, S. Siengchin, *J. Mater. Res. Technol.* **2022**, *18*, 2175.

[15] P. K. Szewczyk, U. Stachewicz, *Adv. Colloid Interface Sci.* **2020**, *286*, 102315.

[16] J. Knapczyk-Korczak, D. P. Ura, M. Gajek, M. M. Marzec, K. Berent, A. Bernasik, J. P. Chiverton, U. Stachewicz, *ACS Appl. Mater. Interfaces* **2020**, *12*, 1665.

[17] J. E. Karbowniczek, K. Berniak, J. Knapczyk-Korczak, G. Williams, J. A. Bryant, N. D. Nikoi, M. Banzhaf, F. de Cogan, U. Stachewicz, *J. Colloid Interface Sci.* **2023**, *650*, 1371.

[18] J. Chen, X. Huang, B. Sun, Y. Wang, Y. Zhu, P. Jiang, *ACS Appl. Mater. Interfaces* **2017**, *9*, 30909.

[19] S. A. Theron, E. Zussman, A. L. Yarin, *Polymer (Guildf).* **2004**, *45*, 2017.

[20] D. P. Ura, U. Stachewicz, *Macromol. Mater. Eng.* **2022**, *307*, 2100843.

[21] K. Tao, G. Sun, C. Feng, G. Liu, Y. Li, R. Chen, J. Wang, S. Han, *Macromol. Rapid Commun.* **2023**, *44*, 202300060.

[22] J. Wang, Q. Li, D. Liu, C. Chen, Z. Chen, J. Hao, Y. Li, J. Zhang, M. Naebe, W. Lei, *Nanoscale* **2018**, *10*, 16868.

[23] Y. Guo, S. Wang, K. Ruan, H. Zhang, J. Gu, *npj Flex. Electron.* **2021**, *5*, 16.

[24] E. A. Sroczyk, J. A. Bryant, F. de Cogan, J. Knapczyk-Korczak, M. M. Marzec, P. K. Szewczyk, M. Banzhaf, U. Stachewicz, *Appl. Surf. Sci.* **2022**, *592*, 153302.

[25] L. Kong, N. Dong, G. Tian, S. Qi, D. Wu, *Appl. Surf. Sci.* **2020**, *511*, 145443.

[26] S. Zheng, J. Dong, X. Zhou, X. Li, X. Zhao, Q. Zhang, *ACS Appl. Polym. Mater.* **2022**, *4*, 4558.

[27] J. Huang, Z. Huang, S. Yi, Y. Liu, M. Fang, S. Zhang, *Sci. Rep.* **2013**, *3*, 3504.

[28] J. E. Karbowniczek, D. P. Ura, U. Stachewicz, *Compos. Part B Eng.* **2022**, *241*, 110011.

[29] A. Doustgani, E. Vasheghani-Farahani, M. Soleimani, S. Hashemi-Najafabadi, *Compos. Part B Eng.* **2012**, *43*, 1830.

[30] J. E. Estevez, B. G. Harvey, G. S. Ostrom, G. H. Hefley, C. G. Yelton, M. D. Garrison, *ACS Appl. Nano Mater.* **2019**, *2*, 7585.

[31] X. Yang, Y. Guo, Y. Han, Y. Li, T. Ma, M. Chen, J. Kong, J. Zhu, J. Gu, *Compos. Part B Eng.* **2019**, *175*, 107070.

[32] J. Zhang, D. Liu, Q. Han, L. Jiang, H. Shao, B. Tang, W. Lei, T. Lin, C. H. Wang, *Compos. Part B Eng.* **2019**, *175*, 107157.
[33] D.-L. Zhang, J.-W. Zha, W.-K. Li, C.-Q. Li, S.-J. Wang, Y. Wen, Z.-M. Dang, *Compos. Sci. Technol.* **2018**, *156*, 1.
[34] H. Wang, Y. Zhang, H. Niu, L. Wu, X. He, T. Xu, N. Wang, Y. Yao, *Compos. Part B Eng.* **2022**, *230*, 109505.
[35] X. Yu, Y. Li, X. Wang, Y. Si, J. Yu, B. Ding, *ACS Appl. Mater. Interfaces* **2020**, *12*, 32078.
[36] J. Chen, X. Huang, B. Sun, P. Jiang, *ACS Nano* **2019**, *13*, 337.
[37] S. Metwally, J. E. Karbowniczek, P. K. Szewczyk, M. M. Marzec, A. Gruszczyński, A. Bernasik, U. Stachewicz, *Adv. Mater. Interfaces* **2019**, *6*, 1801211.
[38] Z. J. Krysiak, Ł. Kaniuk, S. Metwally, P. K. Szewczyk, E. A. Sroczyk, P. Peer, P. Lisiecka-Graca, R. J. Bailey, E. Bilotti, U. Stachewicz, *ACS Appl. Bio Mater.* **2020**, *3*, 7666.
[39] Q. Chen, X. Yan, L. Wu, Y. Xiao, S. Wang, G. Cheng, R. Zheng, Q. Hao, *ACS Appl. Mater. Interfaces* **2021**, *13*, 5435.
[40] Q.-H. Zhu, J.-S. Peng, X. Guo, R.-X. Zhang, L. Jiang, Q.-F. Cheng, W.-J. Liang, *Chinese Phys. B* **2022**, *31*, 108102.
[41] H. Chen, F. Daneshvar, Q. Tu, H.-J. Sue, *ACS Appl. Mater. Interfaces* **2022**, *14*, 56253.
[42] F. Gucmann, J. W. Pomeroy, M. Kuball, *Nano Today* **2021**, *39*, 101206.
[43] Q. Zhang, W. Zhu, J. Zhou, Y. Deng, *Small* **2023**, DOI 10.1002/smll.202300968.
[44] B. Graczykowski, A. El Sachat, J. S. Reparaz, M. Sledzinska, M. R. Wagner, E. Chavez-Angel, Y. Wu, S. Volz, Y. Wu, F. Alzina, C. M. Sotomayor Torres, *Nat. Commun.* **2017**, *8*, 415.
[45] J. Chen, H. Wei, H. Bao, P. Jiang, X. Huang, *ACS Appl. Mater. Interfaces* **2019**, *11*, 31402.
[46] G. Yang, X. Zhang, D. Pan, W. Zhang, Y. Shang, F. Su, Y. Ji, C. Liu, C. Shen, *ACS Appl. Mater. Interfaces* **2021**, *13*, 32286.
[47] B. Yu, J. Fan, J. He, Y. Liu, R. Wang, K. Qi, P. Han, Z. Luo, *J. Alloys Compd.* **2023**, *930*, 167303.
[48] Z. Wei, X. Kong, J. Cheng, H. Zhou, J. Yu, S. Lu, *Compos. Commun.* **2022**, *29*, 101036.
[49] F. Xing, Z. Ou, X. Gao, B. Chen, Z. L. Wang, *Adv. Funct. Mater.* **2022**, *32*, 2205275.
[50] Z. Dai, N. Wang, Y. Yu, Y. Lu, L. Jiang, D.-A. Zhang, X. Wang, X. Yan, Y.-Z. Long, *ACS Appl. Mater. Interfaces* **2021**, *13*, 44234.
[51] P. C. Uzabakiriho, M. Wang, K. Wang, C. Ma, G. Zhao, *ACS Appl. Mater. Interfaces* **2022**, *14*, 46068.
[52] L. Ma, M. Zhou, R. Wu, A. Patil, H. Gong, S. Zhu, T. Wang, Y. Zhang, S. Shen, K. Dong, L. Yang, J. Wang, W. Guo, Z. L. Wang, *ACS Nano* **2020**, *14*, 4716.
[53] G. Guzel Kaya, H. Deveci, *J. Ind. Eng. Chem.* **2020**, *89*, 13.
[54] Y. Zhou, J. Fang, X. Wang, T. Lin, *J. Mater. Res.* **2012**, *27*, 537.
[55] D. Kamireddi, R. M. Street, C. L. Schauer, *Polym. Eng. Sci.* **2023**, *63*, 677.